

Simulating the charging of cylindrical electrolyte-filled pores with the modified Poisson–Nernst–Planck equations

Cite as: J. Chem. Phys. **156**, 214105 (2022); <https://doi.org/10.1063/5.0094553>

Submitted: 04 April 2022 • Accepted: 12 May 2022 • Accepted Manuscript Online: 12 May 2022 •
Published Online: 01 June 2022

Jie Yang,  Mathijs Janssen,  Cheng Lian, et al.



View Online



Export Citation



CrossMark

ARTICLES YOU MAY BE INTERESTED IN

[Dynamic density functional theory for the charging of electric double layer capacitors](#)

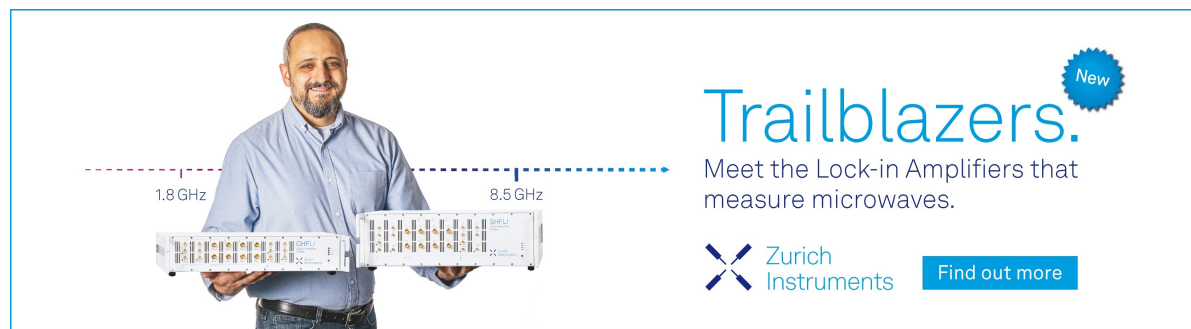
The Journal of Chemical Physics **156**, 084101 (2022); <https://doi.org/10.1063/5.0081827>


[Transition orbital projection approach for excited state tracking](#)

The Journal of Chemical Physics **156**, 214104 (2022); <https://doi.org/10.1063/5.0081207>


[Bayesian, frequentist, and information geometric approaches to parametric uncertainty quantification of classical empirical interatomic potentials](#)

The Journal of Chemical Physics **156**, 214103 (2022); <https://doi.org/10.1063/5.0084988>



Trailblazers. 

Meet the Lock-in Amplifiers that measure microwaves.

 Zurich Instruments [Find out more](#)

Simulating the charging of cylindrical electrolyte-filled pores with the modified Poisson–Nernst–Planck equations

Cite as: J. Chem. Phys. 156, 214105 (2022); doi: 10.1063/5.0094553

Submitted: 4 April 2022 • Accepted: 12 May 2022 •

Published Online: 1 June 2022



View Online



Export Citation



CrossMark

Jie Yang,¹ Mathijs Janssen,^{2,a)} Cheng Lian,^{1,b)} and René van Roij³

AFFILIATIONS

¹School of Chemistry and Molecular Engineering, East China University of Science and Technology, Shanghai 200237, China

²Department of Mathematics, Mechanics Division, University of Oslo, N-0851 Oslo, Norway

³Institute for Theoretical Physics, Center for Extreme Matter and Emergent Phenomena, Utrecht University, Princetonplein 5, 3584 CC Utrecht, The Netherlands

^{a)}Electronic mail: mathijsj@uio.no

^{b)}Author to whom correspondence should be addressed: liancheng@ecust.edu.cn

ABSTRACT

Understanding how electrolyte-filled porous electrodes respond to an applied potential is important to many electrochemical technologies. Here, we consider a model supercapacitor of two blocking cylindrical pores on either side of a cylindrical electrolyte reservoir. A stepwise potential difference 2Φ between the pores drives ionic fluxes in the setup, which we study through the modified Poisson–Nernst–Planck equations, solved with finite elements. We focus our discussion on the dominant timescales with which the pores charge and how these timescales depend on three dimensionless numbers. Next to the dimensionless applied potential Φ , we consider the ratio R/R_b of the pore's resistance R to the bulk reservoir resistance R_b and the ratio r_p/λ of the pore radius r_p to the Debye length λ . We compare our data to theoretical predictions by Aslyamov and Janssen (Φ), Posey and Morozumi (R/R_b), and Henrique, Zuk, and Gupta (r_p/λ). Through our numerical approach, we delineate the validity of these theories and the assumptions on which they were based.

Published under an exclusive license by AIP Publishing. <https://doi.org/10.1063/5.0094553>

I. INTRODUCTION

The dynamics of ions in narrow conducting pores underlies various technologies including biosensors¹ and capacitive energy storage,^{2–4} energy harvesting,⁵ and water deionization.⁶ Many of these technologies are based on charging porous electrolyte-filled electrodes, which is a multi-scale process that involves ionic currents over millimeters in electroneutral reservoirs and micron-sized macropores, to form nanometer-sized electric double layers (EDLs) in the electrodes' pores.⁷ Standard electrochemical techniques such as cyclic voltammetry and impedance spectroscopy characterize the response of a macroscopic electrode–electrolyte system.^{8–10} The microscopic processes underlying charging of pores, possibly of different sizes and shapes, are then measured all at once; disentangling such microscopic information is not straightforward. Experimental insight into the charging dynamics at the single-pore level is, thus, difficult, but progress has been made using nuclear magnetic

resonance experiments (albeit on macroscopic porous electrodes)^{11,12} and with the surface force balance apparatus.¹³ Molecular simulation studies face difficulties opposite to those of experiments as computational power limits simulations to idealized systems of several nanometers at most. Specifically, many molecular dynamics studies considered ionic liquid-filled slit pores with pore widths comparable to the ion diameters;^{14–18} cylindrical pores¹⁹ and realistic (but small) porous structures²⁰ were also studied.

These experiments and simulations are often interpreted using the transmission line (TL) model.^{21–23} This model asserts (i) that the charging of a mesoporous electrode filled with a dilute electrolyte can be characterized through the charging of a single pore and (ii) that the charging of such a pore can be described by an equivalent circuit, the *transmission line circuit*, which distributes the pore's total resistance R and capacitance C over smaller circuit elements. In the limit of infinitely many, infinitesimally small resistors and capacitors, the TL circuit gives rise to the differential “TL equation” [viz.

Eq. (6)] for the local electrostatic potential in the pore.²⁴ The TL equation was solved for semi-infinite pores subject to various time-dependent voltages and currents by Ksenzhek and Stender²² and de Levie.²³ They found that a step potential causes the charge Q on the pore to increase with a power law, $Q \propto \sqrt{t}$. This result can at best represent a short-time regime since, clearly, the charge cannot continue to grow indefinitely. Posey and Morozumi²⁵ solved the TL equation for finite-length pores and found that, on longer timescales, pores charge exponentially with a timescale proportional to RC [see Eq. (9)]. These authors also discussed the influence of a bulk reservoir of resistance R_b with which the pore is in contact. Gupta and co-workers studied a pore with overlapping EDLs, for which they proposed and solved an amended TL equation [see Eq. (17)].^{26,27}

Hundreds of articles have used the TL model and its solutions. Yet, only a handful studied the microscopic physics underlying the TL model—ionic currents in a pore and the EDL formation on its surfaces.^{26–31} Sakaguchi and Baba numerically solved the Poisson–Nernst–Planck (PNP) equations to study a finite-length pore subject to a suddenly-applied potential.²⁸ Their analysis confirmed the short-time power-law scaling but not the exponential relaxation regimes, presumably because ionic charge perturbations did not yet span the entire pore at the latest times they considered [cf. Figs. 1(c) and 1(d) therein]. Mirzadeh *et al.*³¹ also solved the

PNP equations numerically and showed that the TL model accurately describes pore charging for small applied potentials, not only for cylindrical pores but also for other geometries.³¹ Two recent studies further reinforced the TL equation's theoretical basis with first-principles analytical derivations: both starting from the PNP equations, Henrique *et al.*²⁷ derived the TL equation and Aslyamov and Janssen³² derived the finite-length TL results of Posey and Morozumi.

The TL model only applies to pores subject to applied potentials smaller than the thermal voltage (24 mV at room temperature). Several recent articles moved beyond the TL model and studied the response of electrolyte-filled pores subject to larger applied potentials, $\Phi \sim 1$, with Φ the applied potential scaled to the thermal voltage.^{31,33,34} Robinson *et al.* argued that, at large applied potentials, salt depletion from the pores increases their resistivity, slowing down charging.³³ Biesheuvel and Bazant also predicted that, after initial TL-model behavior, a slower exponential relaxation sets in with a timescale characteristic of neutral salt diffusion.³⁴ A charging slowdown with increasing Φ was, indeed, visible in the numerical PNP solutions of Mirzadeh *et al.*,³¹ but the system slowed down less than predicted by Ref. 34. The authors ascribed this discrepancy to surface conduction: for moderate Φ , the EDLs present a shortcut for ions to bypass the dilute center of the pore. Semi-analytical results of Aslyamov and Janssen³² fully agreed with the numerical results of Ref. 31.

The PNP equations do not account for electrostatic correlations and the finite size of the ions, so the validity of the mentioned numerical and analytical studies is limited to cases wherein these effects can be ignored. The point-ion approximation is justified for dilute electrolytes and for $\Phi \sim 1$, but not for concentrated electrolytes or for larger Φ . Accordingly, Niyi and Andrews studied the charging of porous conductive carbon materials³⁵ through the modified Poisson–Nernst–Planck (MPNP) equations.³⁶ Aslyamov *et al.*³⁷ used classical density functional theory to study slit pore charging. They unified all three known charging regimes: the pore's charge first increases as if it was semi-infinite ($Q \propto \sqrt{t}$), then slows down and approaches its equilibrium value exponentially with an RC time, and then slows down even further and equilibrates exponentially with the salt diffusion timescale.³⁷

In this article, we report comprehensive numerical simulations of pore charging using the MPNP equations. We consider many different pore and reservoir sizes, ion diameters, ion concentrations, and applied potentials. We focus our discussion on three dimensionless parameters: the ratio R/R_b of the pore's resistance R to the bulk reservoir resistance R_b , the ratio r_p/λ of the pore radius r_p to the Debye length λ , and the dimensionless applied potential Φ . We compare our numerical solutions to theory predictions from Refs. 24, 25, 27, and 32 that have not been tested before.

II. MODEL

A. Setup

We consider two cylindrical metallic pores of equal length ℓ_p and radius r_p separated concentrically by a cylindrical bulk reservoir of length ℓ_r and radius r_r ; see Fig. 1. At the ends of the pores are caps of length $r_p/5$ with rounded edges of the same radius (the length of the cap is not counted in ℓ_p). We also add two “connecting

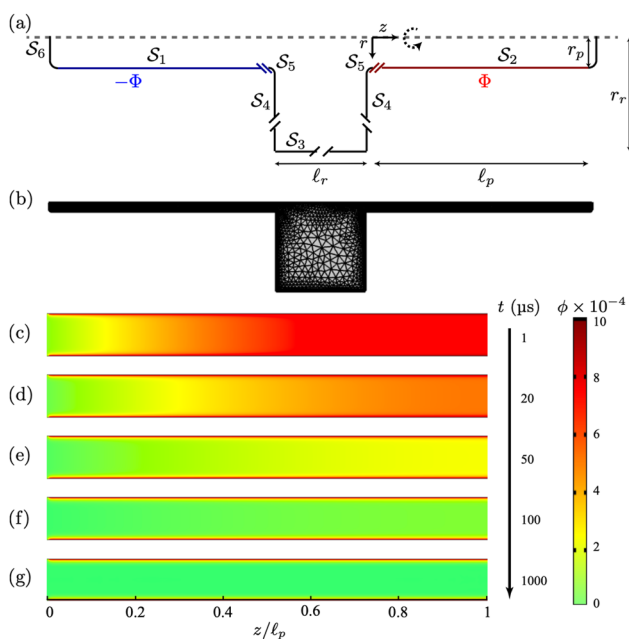


FIG. 1. (a) Section view of the microscopic model of two cylindrical pores of length ℓ_p and radius r_p connected to a cylindrical reservoir of length ℓ_r and radius r_r . The setup is filled with a 1:1 electrolyte (not shown) with ions of diameter a at salt concentration c_b . (b) Representation of a typical mesh to numerically solve the modified Poisson–Nernst–Planck equations. (c)–(g) Heat maps of the local electric potential $\phi(r)$ inside the positive electrode pore at times t after switching on a potential $\Phi = 10^{-3}$ on the electrode, for (c) $t = 1 \mu\text{s}$, (d) $t = 20 \mu\text{s}$, (e) $t = 50 \mu\text{s}$, (f) $t = 100 \mu\text{s}$, and (g) $t = 1000 \mu\text{s}$. We used the ionic diameter $a = 0.1625 \text{ nm}$, bulk salt concentration $c_b = 0.01 \text{ M}$, pore length $\ell_p = 1 \mu\text{m}$, pore radius $r_p = 50 \text{ nm}$, and reservoir length and radius $\ell_r = r_r = 2 \mu\text{m}$.

regions” of smooth corners of radius $r_p/5$ that link the reservoir to the two pores. These regions yield faster convergence of our numerical simulations but have almost no effect on the charging; see Fig. S1 in the [supplementary material](#). For cases wherein the reservoir and pores have the same radius, we exclude the connecting region between the pore and reservoir. We denote the surfaces of the two pores by S_1 and S_2 , the boundaries of the reservoir by S_3 and S_4 , and the boundary of the connecting regions and the caps by S_5 and S_6 . Upon applying a potential between the pores, S_1 and S_2 will acquire opposite electric charge, while S_3 to S_6 remain uncharged. We focus on the charging of the right pore and use a cylindrical coordinate system and a position vector $\mathbf{r} = (r, \theta, z)$ such that $\mathbf{r} = 0$ at the left edge of this pore and such that the z -axis is aligned with the axes of the pores and reservoir.

The reservoir and pores are filled with a 1:1 electrolyte at a bulk ion concentration c_b . The solvent is treated as a structureless continuum of dielectric constant $\epsilon = 6.9 \times 10^{-10} \text{ F m}^{-1}$ and solvent viscosity $\eta = 1.002 \times 10^{-3} \text{ Pa s}^{-1}$ (these values are characteristic for water) at temperature $T = 293 \text{ K}$. The cations and anions carry the charge $+e$ and $-e$, with e being the elementary charge. We set the ionic diffusivity to $D = 1.34 \times 10^{-9} \text{ m}^2 \text{ s}^{-1}$, which is typical for alkali halides in water. For simplicity, neither the concentration dependence nor the effect of confinement is taken into account for the dielectric constant ϵ and the diffusivity D . For future reference, we define two timescales that will appear repeatedly in our discussion,

$$\tau_I = \frac{2\lambda \ell_p^2}{r_p D}, \quad \tau_{II} = \frac{\ell_p^2}{D}, \quad (1)$$

where $\lambda = \sqrt{\epsilon k_B T / (2e^2 c_b)}$ is the Debye length, with k_B being Boltzmann’s constant.

As our setup has a cylindrical symmetry around the z axis, all physical observables are independent of the azimuthal angle θ . We study the time-dependent ionic number densities $\rho_{\pm}(r, z, t)$ —the local ionic concentrations scaled to c_b —and the dimensionless potential $\phi(r, z, t)$ —the local electrostatic potential scaled to the thermal voltage $k_B T/e$. From $\phi(r, z, t)$, we will determine the right pore’s surface charge density,

$$q(z, t) = \frac{\epsilon k_B T}{e} \partial_r \phi(\mathbf{r} \in S_2, t), \quad (2)$$

and its total surface charge,

$$Q(t) = 2\pi r_p \int_{S_2} dz q(z, t). \quad (3)$$

For Eq. (2), we used that $\mathbf{n} \cdot \nabla \phi = -\partial_r \phi$ on S_2 , where \mathbf{n} is the inward normal to the surface.

B. Governing equations

We model $\rho_{\pm}(r, z, t)$ and $\phi(r, z, t)$ through the MPNP equations,

$$\nabla^2 \phi = -\frac{\rho_+ - \rho_-}{2\lambda^2}, \quad (4a)$$

$$\partial_t \rho_{\pm} = -\nabla \cdot \mathbf{j}_{\pm}, \quad (4b)$$

$$\mathbf{j}_{\pm} = -D \left[\nabla \rho_{\pm} \pm \rho_{\pm} \nabla \phi + \frac{a^3 \rho_{\pm} \nabla(\rho_+ + \rho_-)}{1 - a^3(\rho_+ + \rho_-)} \right], \quad (4c)$$

where Eq. (4a) represents the Poisson equation, Eq. (4b) is the continuity equation, and Eq. (4c) is the modified Nernst–Planck equation.³⁶ Here, $\mathbf{j}_{\pm}(r, z, t)$ are the ionic fluxes scaled to c_b .

We consider the pores to be uncharged and the electrolyte to be homogeneous initially. At time $t = 0$, we apply a positive dimensionless potential Φ to the right pore and a negative dimensionless potential $-\Phi$ to the left pore. This yields the following initial and boundary conditions:

$$\rho_{\pm}(\mathbf{r}, t = 0) = 1, \quad (5a)$$

$$\phi(\mathbf{r} \in S_1, t > 0) = -\Phi, \quad (5b)$$

$$\phi(\mathbf{r} \in S_2, t > 0) = \Phi, \quad (5c)$$

$$\mathbf{n} \cdot \mathbf{j}_{\pm}(\mathbf{r} \in \{S_1, S_2, S_3, S_4, S_5, S_6\}, t) = 0, \quad (5d)$$

$$\mathbf{n} \cdot \nabla \phi(\mathbf{r} \in \{S_3, S_4, S_5, S_6\}, t) = 0. \quad (5e)$$

Here, Eq. (5d) signifies that all walls are blocking and Eq. (5e) signifies that surfaces of the caps connecting regions and reservoir boundaries remain uncharged.

Note that the last term in Eq. (4c)—the term that sets MPNP apart from PNP—only contributes significantly to \mathbf{j}_{\pm} for moderate applied potentials ($\Phi \sim 1$ or larger) and is irrelevant for small applied potentials ($\Phi \ll 1$).

C. Numerical implementation

Numerical simulations for various system parameters $c_b, a, \Phi, \ell_p, r_p, \ell_r$, and r_r were performed with COMSOL MULTIPHYSICS 5.4. We used a structured nonuniform computational mesh [see Fig. 1(b)]: coarse in the reservoir domain and finer near all boundaries, where we used a multilayer rectangular grid with a progressively finer layer-to-layer spacing. The maximum element size was $10 \mu\text{m}$, while the minimum ranged from 0.17 to 100 nm in the pore domain depending on the Debye length. The largest salt concentration we considered was $c_b = 0.1\text{M}$, for which $\lambda = 0.959 \text{ nm}$. Hence, the EDL is resolved by at least five grid points.

III. RESERVOIR-DEPENDENT CHARGING

A. TL model

As a first example of numerically-determined pore charging, Figs. 1(c)–1(g) show the dimensionless potential $\phi(r, z, t)$ for five successive times of an electrolyte-filled pore with a bulk concentration $c_b = 0.01\text{M}$ (so that $\lambda = 3.03 \text{ nm}$), ion size $a = 0.1625 \text{ nm}$, pore length $\ell_p = 1 \mu\text{m}$, pore radius $r_p = 50 \text{ nm}$, and reservoir dimensions $\ell_r = 2 \mu\text{m}$ and $r_r = 2 \mu\text{m}$, subject to a small applied potential $\Phi = 10^{-3}$. At early times, $\phi(r, z, t)/\Phi = 1$ in most of the pore, which implies that the pore’s surface charge density and electric field in the pore are both zero. However, near the reservoir, a finite electric field drives counterions into the pore and coions out of it. At later times, EDLs form in the nanometer vicinity of the pore surfaces, their width set by the Debye length λ , and the potential $\phi(r, z, t)$ decreases until it is zero everywhere except in the EDLs.

The TL model was developed to describe the charging of such pores. However, instead of the full dimensionless potential $\phi(r, z, t)$, the TL equation

$$RC\partial_t\psi = \ell_p^2\partial_z^2\psi, \quad 0 < z < \ell_p, \quad (6)$$

only captures the evolution of $\psi(z, t) = \phi(r = 0, z, t)$ at the pore's centerline. In our case of a cylindrical pore, the pore's resistance amounts to $R = \rho\ell_p/(\pi r_p^2)$, with $\rho = \lambda^2/(\epsilon D)$ being the electrolyte resistivity. For thin EDLs and small Φ , the pore's Helmholtz capacitance amounts to $C = 2\pi r_p \ell_p \epsilon/\lambda$. Their product RC equals τ_I as defined in Eq. (1). For this reason, τ_I is known as the TL timescale.³¹ However, this is a bit misleading as the dominant relaxation timescale of a finite-length pore actually also depends on the parameters of the reservoir with which it is in contact.^{24,25} Here, the bulk resistance R_b dependence enters the problem through the boundary conditions to which Eq. (6) is subject,^{24,25,34} viz.,

$$\psi(z, 0) = \Phi, \quad 0 < z < \ell_p, \quad (7a)$$

$$\ell_p\partial_z\psi(0, t) = \frac{R}{R_b}\psi(0, t), \quad (7b)$$

$$\partial_z\psi(\ell_p, t) = 0. \quad (7c)$$

Here, Eq. (7a) describes the initial condition, Eq. (7b) expresses Kirchhoff's current law at the reservoir–pore interface, and Eq. (7c) accounts for the blocking wall at the end of the pore.

For our setup, the bulk resistance $R_b = R_r + R_c$ consists of two parts, i.e., the resistance $R_r = \rho\ell_r/(2\pi r_r^2)$ of half of the reservoir and the resistance R_c of the connecting region. This connecting region is bordered by rounded edges of radius $r_p/5$ centered around $z = 0$. The z -dependent radius $r_c(z)$ of the connecting region thus satisfies $z^2 + (r_c - 6r_p/5)^2 = r_p^2/5^2$. To find R_c , we view the connecting region as a stack of cylindrical slabs of infinitesimal thickness dz and resistance $\rho dz/A$, with $A = \pi r_c^2$. We then find $R_c = \rho \int_{-r_p/5}^0 dz/[\pi r_c(z)]^2$, which, upon writing $\bar{z} = z/r_p$, yields

$$R_c = \frac{\rho}{\pi r_p} \int_{-\frac{1}{5}}^0 d\bar{z} \left(6/5 + \sqrt{1/5^2 - \bar{z}^2}\right)^{-2} \approx \frac{\rho}{\pi r_p} \times 0.109. \quad (8)$$

We, thus, find $R_b = R_r(1 + R_c/R_r)$, where $R_c/R_r \approx 0.218 \times r_r^2/(r_p\ell_r)$. In our calculations below, this term varies between $R_c/R_r = 1.09$ (for $r_r = \ell_r = 1 \mu\text{m}$ and $r_p = 200 \text{ nm}$) and $R_c/R_r = 54.5$ (for $r_r = \ell_r = 50 \mu\text{m}$ and $r_p = 200 \text{ nm}$). Hence, for very wide reservoirs, the tiny connecting region can constitute the major part of the bulk resistance, $R_b \approx R_c$. However, the pore's resistance is always vastly larger than that of the connecting region, $R_c \ll R$, so in cases where $R_b \approx R_c$, we have $R_b \ll R$.

Posey and Morozumi solved Eqs. (6) and (7) (albeit in different notation) and found²⁵

$$\frac{\psi(z, t)}{\Phi} = \sum_{j=1}^{\infty} \frac{4 \sin \beta_j \cos [\beta_j(1 - z/\ell_p)]}{2\beta_j + \sin 2\beta_j} \exp\left(-\frac{t}{\tau_j}\right), \quad (9a)$$

with timescales $\tau_j = \tau_I/\beta_j^2$ and β_j solutions of

$$\beta_j \tan \beta_j = \frac{R}{R_b}. \quad (9b)$$

As discussed in Ref. 24, the early-time charging behavior of the TL, Eq. (6), is not affected by the Neumann boundary condition,

Eq. (7c), which, for all practical purposes, can be taken toward $\ell_p \rightarrow \infty$. A solution to the TL equation for these settings was presented in Eq. (6) of Ref. 24,

$$\begin{aligned} \frac{\psi(z, t)}{\Phi} = & 1 - \operatorname{erfc} \sqrt{\frac{z^2 RC}{\ell_p^2 4t}} \\ & + \exp\left(\frac{R}{R_b} \frac{z}{\ell_p} + \frac{R^2 t}{R_b^2 RC}\right) \\ & \times \operatorname{erfc}\left(\sqrt{\frac{z^2 RC}{\ell_p^2 4t}} + \frac{R}{R_b} \sqrt{\frac{t}{RC}}\right). \end{aligned} \quad (10)$$

We find the total surface charge $Q(t) = -\int_0^t dt' I(t')$ on the pore, with $I(t) = -(k_B T/e)\ell_p\partial_z\psi(0, t)/R$ the ionic current into the pore, as

$$\begin{aligned} Q(t) = & \frac{k_B T}{e} C\Phi \left[\sqrt{\frac{4t}{\pi RC}} - \frac{R_b}{R} \right. \\ & \left. + \frac{R_b}{R} \exp\left(\frac{R^2 t}{R_b^2 RC}\right) \operatorname{erfc}\left(\frac{R}{R_b} \sqrt{\frac{t}{RC}}\right) \right]. \end{aligned} \quad (11)$$

When the bulk resistance is negligible compared to the resistance of the pore, $R \gg R_b$, Eq. (11) reduces to

$$Q(t) = \frac{k_B T}{e} C\Phi \sqrt{\frac{4t}{\pi RC}}, \quad (12)$$

which is the $\propto \sqrt{t}$ behavior discussed before.²⁸ When the reservoir resistance is not small, $R \sim R_b$, we find the early-time behavior by expanding Eq. (11) for $t/(RC) \ll 1$,

$$Q(t) = \frac{k_B T}{e} \frac{\Phi}{R_b} \left[t + O(t^{3/2}) \right]. \quad (13)$$

B. Comparing numerical MPNP solutions to TL-model predictions

We numerically solve Eqs. (4) and (5) for a narrow reservoir ($R/R_b = 2$) and a wide reservoir ($R/R_b = 420.16$) and plot the resulting centerline potential $\phi(r = 0, z, t)$ in Fig. 2 (solid lines). In the same figure, we plot Eq. (9) (dashed lines). In both panels, we see that, from $t = 10^{-4}$ s onward, Eq. (9) agrees well with the numerical data although slightly better for the narrower reservoir. The early times $t = 10^{-7}$ and 10^{-5} s are captured much worse, especially near the pore mouth at $z = 0$. We also show the centerline potential $\phi(r = 0, z, t = 0)$ (black lines) at the moment of switching on the potential difference. To determine $\phi(r = 0, z, t = 0)$, rather than Eqs. (4) and (5), we solved the Laplace equation

$$\nabla^2 \phi(r, z, t) = 0, \quad (14a)$$

$$\phi(\mathbf{r} \in \mathcal{S}_1, t > 0) = -\Phi, \quad (14b)$$

$$\phi(\mathbf{r} \in \mathcal{S}_2, t > 0) = \Phi, \quad (14c)$$

$$\mathbf{n} \cdot \nabla \phi(\mathbf{r} \in \{\mathcal{S}_3, \mathcal{S}_4, \mathcal{S}_5\}, t > 0) = 0, \quad (14d)$$

which is based on the right-hand side of the Poisson Eq. (4a) being zero at $t = 0$. Figure 2(a) shows that the potential in the reservoir

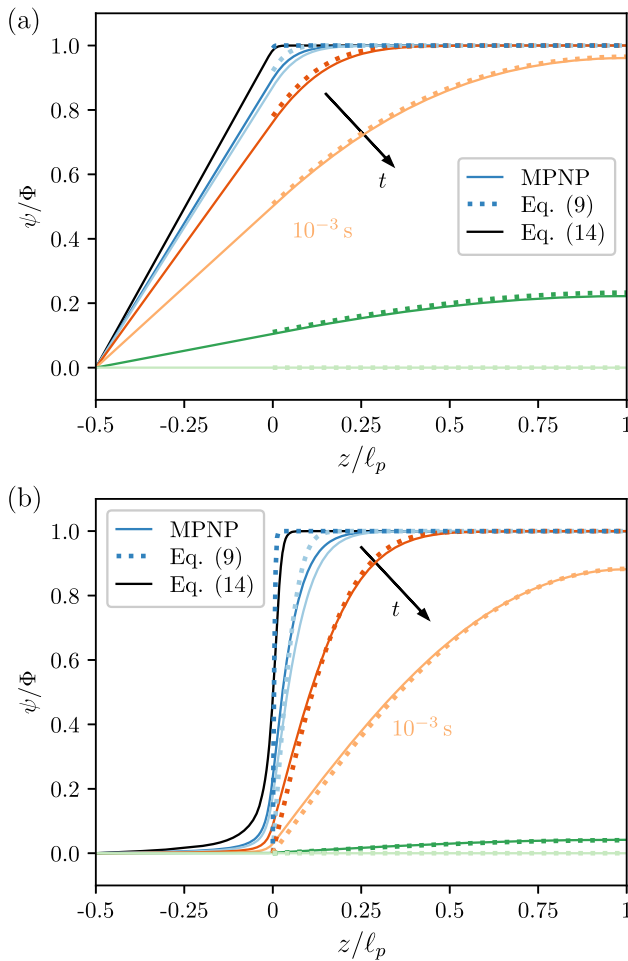


FIG. 2. Position dependence of the relative potential on the central axis at different times after switching on a voltage (a) for a narrow reservoir $r_r = r_p$ and in (b) for a wide reservoir $r_r = 50r_p$ (b). The other parameters are set to $\Phi = 10^{-3}$, $r_p = 200$ nm, $\ell_p = \ell_r = 10$ μm , and $c_b = 0.001$ M. We show numerical solutions to the MPNP Eq. (4) for $t = 10^{-7}, 10^{-5}, 10^{-4}, 10^{-3}, 10^{-2}$, and 10^{-1} s (solid colored lines) and analytical predictions from Eq. (9) (dashed lines) for the same times. We also show a numerical solution to the Laplace equation Eq. (14) (black), which corresponds to $t = 0$.

is linear in the special case $r_r = r_p$, but not if the reservoir is much wider than the pore, as in Fig. 2(b). This may be one reason causing the worse performance of the TL model for the wide reservoir, as Refs. 27 and 34 motivated Eq. (7b) by the potential being linear in the reservoir. As Eq. (7b) can also be derived directly from the TL circuit—containing a single resistor to model the whole bulk reservoir²⁴—we conclude that this circuit does not capture the early-time charging of pores coupled to wide reservoirs. Next, the black line in Fig. 2(b) shows that the potential in the pore ($0 < z < \ell_p$) deviates from $\psi(z = 0, t) = \Phi$ at $t = 0$. Hence, the initial condition, Eq. (7a), used in the TL model does not correspond to the numerical simulations. The discrepancy between Eq. (9) and the MPNP at early times must, therefore, at least be partially caused by the inaccurate initial condition, Eq. (7a).

Figure 3 shows the early-time behavior of $Q(t)$ for the same parameters as we used in Fig. 2. Here, the black line corresponds to $r_r = 10$ μm , for which $R/R_b = 420.16$, and the red line corresponds to $r_r = 200$ nm, for which $R/R_b = 2$. Square-root charging ($Q \propto \sqrt{t}$) is visible for $r_r = 10$ μm up to about $t = 10^{-2}$ s, when the exponential charging starts. This square-root charging is in line with the theoretical prediction Eq. (12) for $R/R_b \gg 1$. For $r_r = 200$ nm, the early-time charge accumulation scales linearly, in line with Eq. (13) for $R/R_b \sim 1$.

C. Dependence of the charging time on R/R_b

We further study the dependence of the charging time of pore charging on the size of the reservoir. Figure 4(a) shows the normalized surface charge $Q(t)/Q_{\text{eq}}$ as a function of time for different reservoir radii r_r and lengths ℓ_r ; the legend is arranged in the order of increasing $R_r = \rho \ell_r / (2\pi r_r^2)$. Here, Q_{eq} is the charge $Q(t)$ at the final timestep. We further set $r_p = 200$ nm and $c_b = 10^{-3}$ M such that $\lambda/r_p = 20.7$; hence, the EDLs are nonoverlapping. In the figure, we see that $Q(t)/Q_{\text{eq}}$ does not vanish at $t = 0$, which was already suggested by the aforementioned deviations from $\psi(z = 0, t = 0) = \Phi$ in Fig. 2(b). Charging relaxation curves overlap for the six smallest R_r , implying that the reservoir has no significant influence. Conversely, for the three largest reservoir resistances, the charging is increasingly slow. This slowdown is also visible in Fig. 4(b), where we plot the same data now as $\ln(1 - Q(t)/Q_{\text{eq}})$. The data in Fig. 4(b) vary linearly vs time on timescales τ_l [Eq. (1)], indicating that the surface charge relaxes exponentially on this timescale. To characterize this exponential charging in more detail, we introduce the instantaneous numerical relaxation-time function,

$$\tau_{\text{num}}(t) = \left[\frac{d \ln(1 - Q(t)/Q_{\text{eq}})}{dt} \right]^{-1}. \quad (15)$$

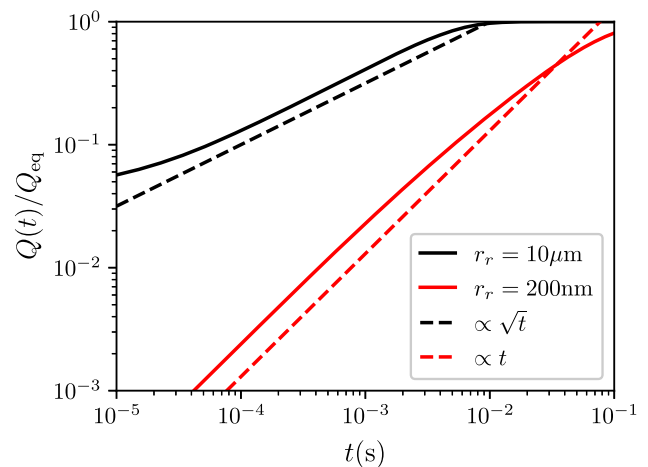


FIG. 3. Log-log plots of the normalized surface charge density $Q(t)/Q_{\text{eq}}$, for a wide reservoir with $r_r = 10$ μm (black) and a narrow reservoir with $r_r = 200$ nm (red). The other parameters are set to $c_b = 10^{-3}$ M, $\ell_p = 10$ μm , $r_p = 200$ nm, $\Phi = 10^{-3}$, $a = 0.1625$ nm, and $\ell_r = 10$ μm .

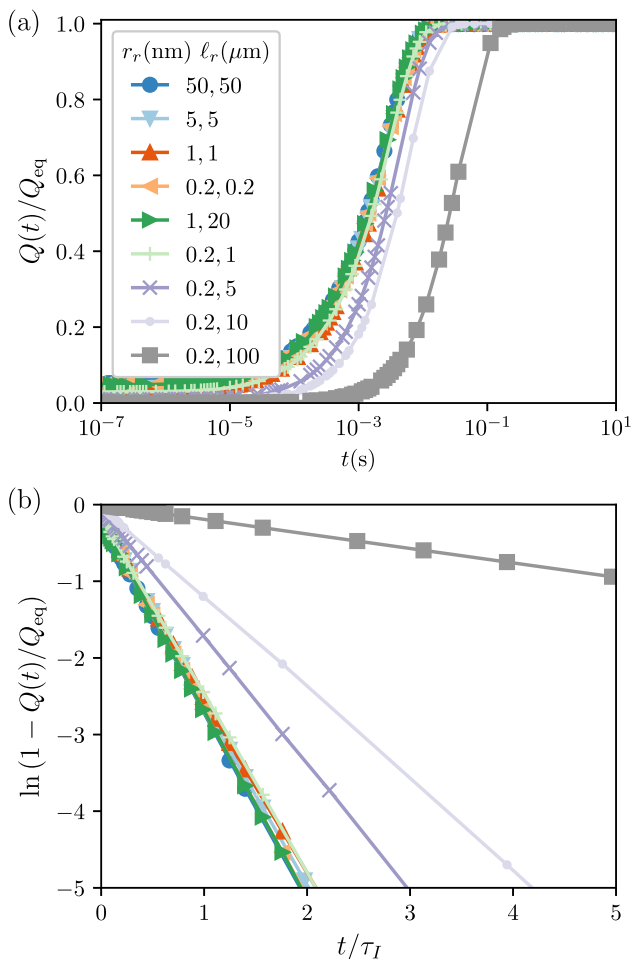


FIG. 4. (a) The normalized surface charge density $Q(t)/Q_{eq}$ vs time, and the (b) surface charge relaxation vs time scaled by τ_I for different reservoir radii r_r and lengths l_r . The other parameters are set to $l_p = 10 \mu\text{m}$, $r_p = 200 \text{ nm}$, $\Phi = 10^{-3}$, $a = 0.1625 \text{ nm}$, and $c_b = 10^{-3} \text{ M}$.

For a purely exponential charging process, $\tau_{num}(t)$ takes a constant value. In reality, however, $\tau_{num}(t)$ is time dependent: Fig. 5(a) shows the instantaneous relaxation time function $\tau_{num}(t)$, Eq. (15), for several reservoir radii r_r and lengths l_r corresponding to the same parameters of Fig. 4. We see that $\tau_{num}(t)$ grows during the early power-law charging (see Fig. 3) until it reaches a plateau around $t = 10^{-3} - 10^{-1} \text{ s}$ whose height we denote by $\bar{\tau}$. (At late times, $Q(t) \approx Q_{eq}$ and the numerical derivative becomes erratic.) We found that we can effectively determine $\bar{\tau}$ from the intersections of $\tau_{num}(t)$ with t (red dashed lines) at which time $\tau_{num} = \bar{\tau}$. Figure 5(b) shows $\bar{\tau}/\tau_I$ vs R_b/R (red triangles) determined in this way. We see that $\bar{\tau}/\tau_I$ does not depend on R_b/R for small values thereof and increases linearly with R_b/R at large values. In the same panel, we show the late-time relaxation timescale $\tau_1 = \tau_I/\beta_1^2$ of Eq. (9) (black line), for which we numerically solved transcendental Eq. (9b). Reference 24 showed that τ_1 can also be decently approximated by

$$\tau_1 \approx RC \left(\frac{4}{\pi^2} + \frac{R_b}{R} \right). \quad (16)$$

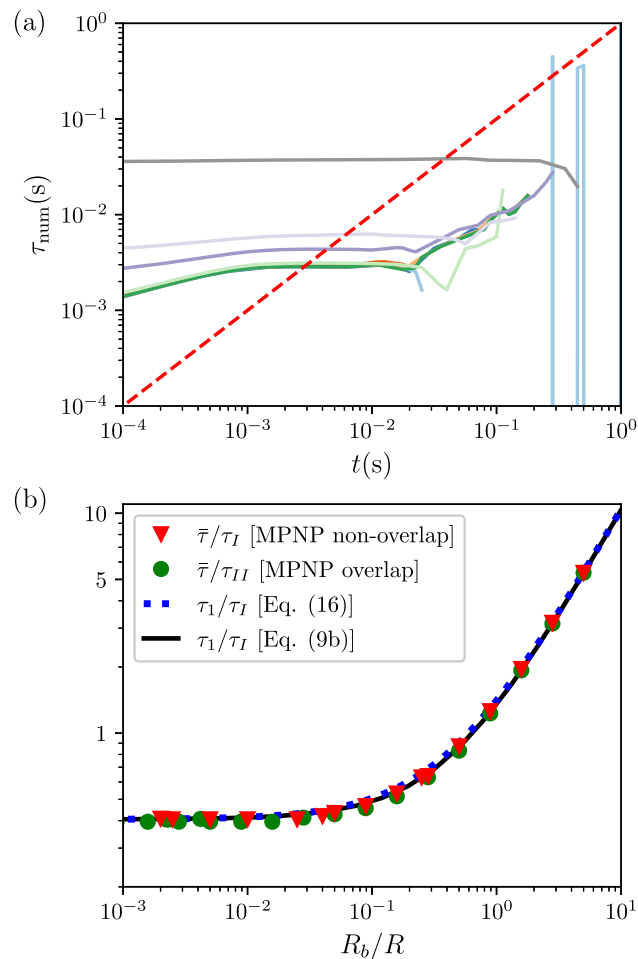


FIG. 5. (a) The instantaneous relaxation time $\tau_{num}(t)$ vs time, using the same line styles and parameters as in Fig. 4, and (b) corresponding numerical charging timescale $\bar{\tau}$ scaled by τ_I (red triangles) vs the ratio of reservoir resistance to pore resistance R_b/R . The other parameters are set to $l_p = 10 \mu\text{m}$, $r_p = 200 \text{ nm}$, $\Phi = 10^{-3}$, $a = 0.1625 \text{ nm}$, and $c_b = 10^{-3} \text{ M}$. We also show a case with overlapping EDLs (green dots) for which $c_b = 10^{-6} \text{ M}$. Finally, we show theoretical predictions from Eq. (16) (dashed blue line) and Eq. (9b) (black line).

Figure 5(b) shows that both τ_1 determined numerically from Eq. (9b) and its approximation [Eq. (16)] (blue dashed line) agree well with $\bar{\tau}(t)$.

Instead of τ_1 , Posey and Morozumi studied the time at which their $\psi(z = l_p, t)$ curve inflected. Their Fig. 10 of this “delay time” vs $\log(R_b/R)$ is constant for $R_b/R \ll 1$ and increases $R_b/R \gg 1$. Our Fig. 5(b) (and Fig. 3 of Ref. 24) is thus related but not identical to Posey and Morozumi’s Fig. 10.

IV. DEPENDENCE ON EDL OVERLAP λ/r_p

A. Theory

Recent work by Fernandez *et al.*²⁷ generalized the TL model to arbitrary values of λ/r_p . They found the following centerline potential:

$$\frac{\psi(z, t)}{\Psi} = I_0\left(\frac{r_p}{\lambda}\right)^{-1} + \left[1 - I_0\left(\frac{r_p}{\lambda}\right)^{-1}\right] \times \sum_{j \geq 1} \frac{4 \sin \beta_j \cos[\beta_j(1 - z/\ell_p)]}{2\beta_j + \sin 2\beta_j} \exp\left(-\frac{t}{\tau_j}\right), \quad (17a)$$

where the timescales τ_j with $j = 1, 2, \dots$ read

$$\tau_j = \frac{I_1(r_p/\lambda)}{I_0(r_p/\lambda)} \frac{\tau_I}{\beta_j^2}, \quad (17b)$$

where I_0 and I_1 are modified Bessel functions of the first kind and where β_j are the solutions of

$$\beta_j \tan \beta_j = \frac{\ell_p r_s^2}{\ell_s r_p^2}. \quad (17c)$$

In Eq. (17c), ℓ_s and r_s are the length and radius of a “stagnant diffusion layer” (SDL), a thin region in the reservoir next to the pore over which the potential supposedly drops to zero. As already noted in Ref. 27, the right-hand side of Eq. (17c) is effectively a ratio R/R_{SDL} of the pore resistance to the SDL resistance. As we did not account for any physical mechanisms (e.g., convection) by which the potential would drop to zero faster than at the center of our reservoir, in Sec. II, we preferred using the reservoir size *in lieu* of the SDL width. In other words, we prefer replacing R_{SDL} by R_b . With this identification, we see that Eq. (17) reduces to Eq. (9) when $r_p \gg \lambda$.

Reference 27 already plotted $\psi(z, t)$ from Eq. (17) vs z for several times and found good agreement with numerical solutions of the PNP equations. Here, we discuss the dependence of the late-time relaxation time τ_1 on the various system parameters.

B. R/R_b dependence for $\lambda/r_p \gg 1$

When $\lambda/r_p \gg 1$, we have that $I_1(r_p/\lambda)/I_0(r_p/\lambda) \approx r_p/(2\lambda)$ so that the late-time relaxation time can be determined from Eq. (17b) as $\tau_1 = \tau_{II}/\beta_1^2$. We solved the MPNP equations for different ℓ_r and r_r and we set $\ell_p = 10 \mu\text{m}$, $c_b = 10^{-6} \text{M}$, and $r_p = 200 \text{nm}$, so that $r_p/\lambda = 0.66$. From these numerical solutions, we determined $\bar{\tau}/\tau_{II}$, which we plot with green dots in Fig. 5(b). We see that these scaled data overlap with the $\bar{\tau}/\tau_I$ data determined in Sec. III C for $\lambda/r_p \ll 1$.

C. λ/r_p dependence for $R/R_b \gg 1$

Next, we considered many different c_b, r_p, ℓ_p , and a . In all cases, $R/R_b \gg 1$; the smallest value considered was $R/R_b \approx 193.80$. For such large R/R_b , we can use that in the limit of $R/R_b \rightarrow \infty$; Eq. (17c) is solved by $\beta_1 = \pi/2$ and

$$\tau_1 = \frac{4}{\pi^2} \frac{I_1(r_p/\lambda)}{I_0(r_p/\lambda)} \tau_I. \quad (18)$$

First, we investigate how the electrolyte concentration affects the charging dynamics. Figure 6 shows the surface charge density $Q(t)/Q_{\text{eq}}$ vs time for several c_b . We see that charging goes faster at higher electrolyte concentrations, which agrees with the τ_I timescale [Eq. (1)] from TL theory. Moreover, this panel shows that the charge data collapse for concentrations below 10^{-5}M , for which Debye lengths are comparable to or larger than the pore radii.

We then drew figures similar to Fig. 6 for cases wherein we varied ℓ_p, r_p , and a ; see panels (a), (b), (d), (e), (g), and (h) of Fig. S2 in the supplementary material. From these data, we determined the respective numerical charging timescales $\bar{\tau}$, which we have collected in Fig. 7(a). We see there that $\bar{\tau}$ is independent of c_b for dilute electrolytes, while $\bar{\tau} \sim c_b^{-0.5}$ for concentrated electrolytes. Moreover, the numerical relaxation time vs electrolyte concentration for three ion diameters $a = [0.1625, 0.3, 0.5] \text{nm}$ and a pore size of $\ell_p = 10 \mu\text{m}$ and $r_p = 200 \text{nm}$ collapse onto a single curve in Fig. 7(a). The independence of the charging process on the ion diameter is also visible in the supplementary material in Figs. S2(g)–S2(i), where $Q(t)/Q_{\text{eq}}$ and $\bar{\tau}$ are unaffected by a over a wide a -range. This independence is easy to understand: for the small potential $\Phi = 10^{-3}$ considered here and in Fig. S2, MPNP and PNP are essentially the same, and PNP does not depend on a . Next, Fig. 7(b) presents the same $\bar{\tau}$ data as Fig. 7(a), but now normalized by τ_I [Eq. (1)] and now vs r_p/λ . With this scaling, data for the different pore sizes and ionic diameters collapse onto a single curve that accurately agrees with τ_1/τ_I from Eq. (18). To understand Fig. 7(b) qualitatively, note that the ratio of Bessel functions in Eq. (18) behaves as

$$\frac{I_1(r_p/\lambda)}{I_0(r_p/\lambda)} = \begin{cases} \frac{r_p}{2\lambda} & \text{for } r_p \ll \lambda, \\ 1 & \text{for } r_p \gg \lambda. \end{cases} \quad (19)$$

With Eq. (18), we then find

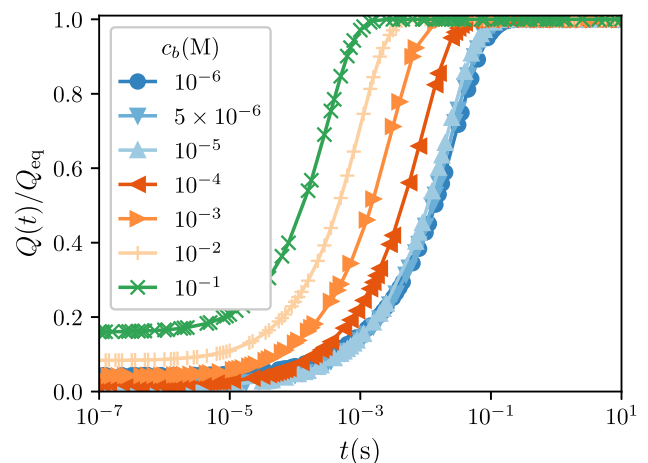


FIG. 6. The normalized surface charge density $Q(t)/Q_{\text{eq}}$ vs time for various electrolyte concentrations of $c_b = (10^{-6} - 4) \text{M}$, with τ_I given by Eq. (1). The other parameters are set to $\ell_p = 10 \mu\text{m}$, $r_p = 200 \text{nm}$, $a = 0.1625 \text{nm}$, $\Phi = 10^{-3}$, $\ell_r = 10 \mu\text{m}$, and $r_r = 10 \mu\text{m}$.

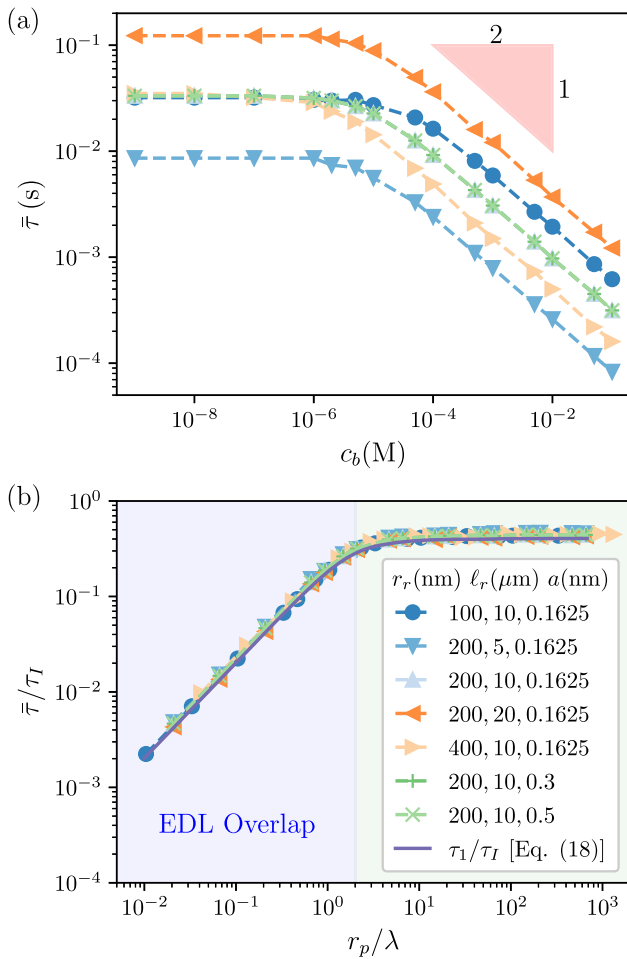


FIG. 7. (a) Numerical relaxation $\bar{\tau}$ of our pore setup for $\Phi = 10^{-3}$ and various pore sizes and ion diameters a , plotted against c_b . Panel (b) shows the same data as (a), normalized by τ_I and plotted against r_p/λ . The reservoir size was set to $\ell_r = 10 \mu\text{m}$ and $r_r = 10 \mu\text{m}$. The legend in panel (b) also applied to panel (a).

$$\frac{\tau_1}{\tau_I} = \frac{4}{\pi^2} \times \begin{cases} \frac{r_p}{2\lambda} & \text{for } r_p \ll \lambda, \\ 1 & \text{for } r_p \gg \lambda, \end{cases} \quad (20)$$

which agrees with the scaling observed in Fig. 7(b).

The r_p/λ -dependent charging dynamics of our pore-reservoir-pore setup is reminiscent of the charging of an electrolyte between two planar electrodes separated by a distance L —for which L/λ is a key parameter. For the latter setup, the linearized PNP equations can be solved with a Laplace transformation, which was first done approximately by Bazant *et al.*³⁸ and later exactly by Janssen and Bier³⁹ and Palaia.⁴⁰ In particular, Ref. 39 predicted the following late-time relaxation timescale,

$$\tau_p = \frac{\lambda^2}{D(1 + \mathcal{M}_1^2 \lambda^2/L^2)}, \quad (21a)$$

$$\mathcal{M}_1 \equiv \begin{cases} M_1 & \text{for } L/\lambda < \sqrt{3}, \\ i\tilde{m}_1 & \text{for } L/\lambda > \sqrt{3}, \end{cases} \quad (21b)$$

where M_1 and \tilde{m}_1 are the smallest solutions of two transcendental equations,

$$\tan M = M(1 + M^2 \lambda^2/L^2), \quad (21c)$$

$$\tanh \tilde{m} = \tilde{m}(1 - \tilde{m}^2 \lambda^2/L^2). \quad (21d)$$

Equation (21) has the following limiting behavior:

$$\tau_p = \begin{cases} \frac{4L^2}{\pi^2 D} [1 + O(L/\lambda)^2] & \text{for } L/\lambda \ll \sqrt{3}, \\ \frac{\lambda L}{D} [1 + O(\lambda/L)] & \text{for } L/\lambda \gg \sqrt{3}. \end{cases} \quad (22)$$

For four values between $L/\lambda = 11$ and 32, Asta *et al.*⁴¹ showed with lattice Boltzmann electrokinetics simulations that Eq. (21) predicted the relaxation timescale more accurately than the well-known RC time $\lambda L/D$. To our knowledge, the predictions of Refs. 39 and 40 for $L/\lambda < 1$ have not been numerically tested. Therefore, we used the same MPNP implementation as before to simulate the charging dynamics of two flat plates over a wide range of L and c_b . Figure 8(a) shows numerical results for the numerical charging timescale $\bar{\tau}$. We observe that $\bar{\tau} \sim c_b^{-0.5}$ for most cases except for extremely dilute electrolytes in narrow confinement. Figure 8(b) shows that the same data collapse onto a single curve when we scale $\bar{\tau}$ by $\lambda L/D$ and plot these data against L/λ . The data (symbols) in this panel agree excellently with the theoretical prediction of Eq. (21) (line).

V. CHARGING AT MODERATE APPLIED POTENTIALS $\Phi \sim 1$

Porous electrodes subject to moderate to large potentials are known to acquire charge “biexponentially,” that is, the surface charge is a sum of (at least) two exponential functions with two different timescales.^{7,14,17,34,37,42} From the modeling point of view, relaxation of porous electrodes on two timescales was first predicted by Biesheuvel and Bazant.³⁴ Mirzadeh and co-workers numerically solved the PNP equations and found the outcome of biexponential charge buildup—namely, charging slowdown—but did not disentangle the two exponential regimes. Aslyamov and Janssen³² studied a slit pore of width H with thin EDLs ($H \gg \lambda$), for which they derived

$$\frac{Q(t)}{Q_{\text{eq}}} \simeq 1 - \frac{8}{\pi^2} \left[\exp\left(-\frac{\pi^2}{4} \frac{1}{\cosh(\Phi/2)} \frac{t}{\tau_I}\right) + \frac{4\lambda}{H} \sinh^2\left(\frac{\Phi}{4}\right) \exp\left(-\frac{\pi^2}{4} \frac{t}{\tau_{II}}\right) \right] + O(\eta^2), \quad (23)$$

where the discarded higher-order terms involve a Dukhin number,

$$\eta = 4 \exp\left(\frac{\Phi}{2}\right) \frac{\lambda}{r_p}. \quad (24)$$

For the thin EDLs considered in Ref. 32, $\tau_{II} \gg \tau_I$ [cf. Eq. (1)], which means that Eq. (23) predicts relaxation on two well-separated

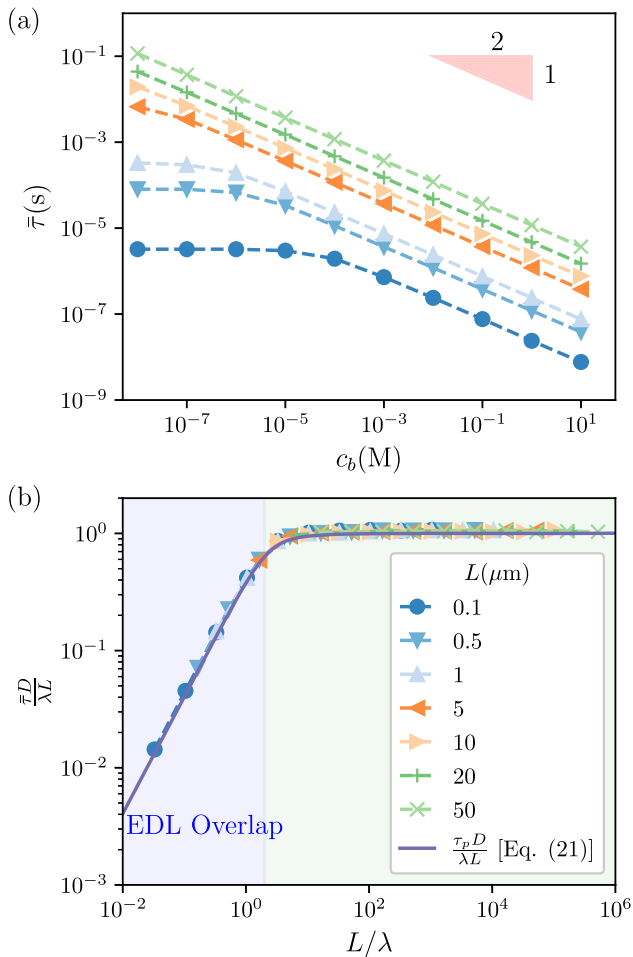


FIG. 8. (a) Numerical relaxation $\bar{\tau}$ for planar electrodes subject to $\Phi = 10^{-3}$ with various separated distance L plotted against c_b . (b) The same data in (a) normalized by $\lambda L/D$, plotted against L/λ .

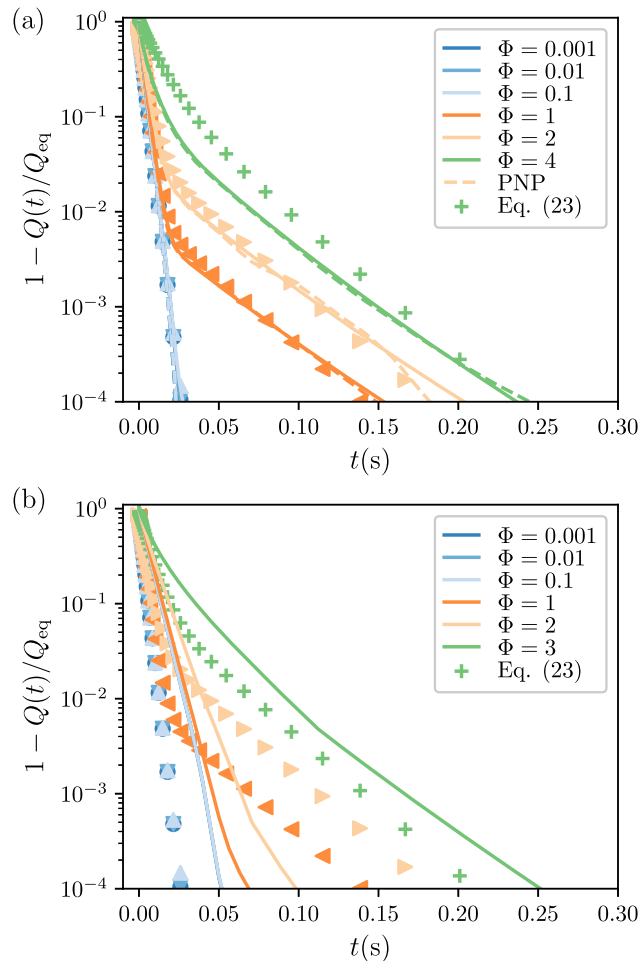


FIG. 9. Surface charge relaxation at different values of applied potentials Φ and for different reservoir sizes of (a) $r_r = 10 \mu\text{m}$ and (b) $r_r = 200 \text{ nm}$. Lines represent results from MPNP, dashed lines represent results from PNP, and dots portray Eq. (23). Parameters are set to $\ell_p = 10 \mu\text{m}$, $\ell_r = 10 \mu\text{m}$, $a = 0.1625 \text{ nm}$, $r_p = 200 \text{ nm}$, and $c_b = 10^{-3} \text{ M}$, such that $r_p/\lambda = 20.7$, i.e., nonoverlapping EDLs.

timescales (unless $\Phi \gg 1$). The second exponential term goes with exactly the same timescale as we found in Eqs. (17) and (20). In these equations, however, the τ_{II} timescale was caused by EDL overlap, while, here, it is caused by moderate applied potentials. Note that, in Eqs. (23) and (24), we replaced the pore width H of Ref. 32 by our pore radius r_p . We did this because a slit and a cylindrical pore have hydraulic radii $H/2$ and $r_p/2$,³⁰ respectively, so that H and r_p play similar roles.

Figure 9 shows the charge buildup of our setup (lines) for $\Phi = 0.001, 0.01, 0.1, 1, 2$, and 4 for a wide reservoir ($r_r = 10 \mu\text{m}$) (a) and a narrow reservoir ($r_r = 200 \text{ nm}$) (b) as determined numerically solving the MPNP equations. We also plot Eq. (23) (symbols) for the same Φ . For the wide reservoir [Fig. 9(a)], the numerics agree with Eq. (23) well except for $\Phi = 4$. We see that, up to about $t = 0.05 \text{ s}$, $1 - Q(t)/Q_{\text{eq}}$ relaxes exponentially with a Φ -dependent slope, in agreement with the first line of Eq. (23). (For $\Phi = 4$, the slowdown is less than predicted.) Thereafter, a second, slower exponential

relaxation emerges, which becomes more important with increasing Φ , in line with the $\sinh^2(\Phi/4)$ term in Eq. (23).

While Eq. (23) was derived from the PNP equations, the other data in Fig. 9 were determined numerically from the MPNP equations. For comparison, we also show numerical solutions of the PNP equations [Eq. (4) without the last term of Eq. (4c)] with dashed lines in Fig. 9(a). The data for $1 - Q(t)/Q_{\text{eq}}$ are almost the same for PNP and MPNP. This is not surprising as, for the $a = 0.1625 \text{ nm}$ and $c_b = 10^{-3} \text{ M}$ considered here, we have volume fraction $v = 2a^3 c_b = 5.17 \times 10^{-6}$; Fig. (5) of Ref. 43 shows that the capacitance of the modified and regular Poisson Boltzmann theory hardly differs for $\Phi < 10$ for such a small v . Concluding, the difference between PNP and MPNP does not explain the discrepancy between the dots and lines in Fig. 9(a) at $\Phi = 4$.

From Eq. (24), we see that the accuracy of Eq. (23) depends both on the surface potential and the EDL overlap. For $\Phi = 2$, we find

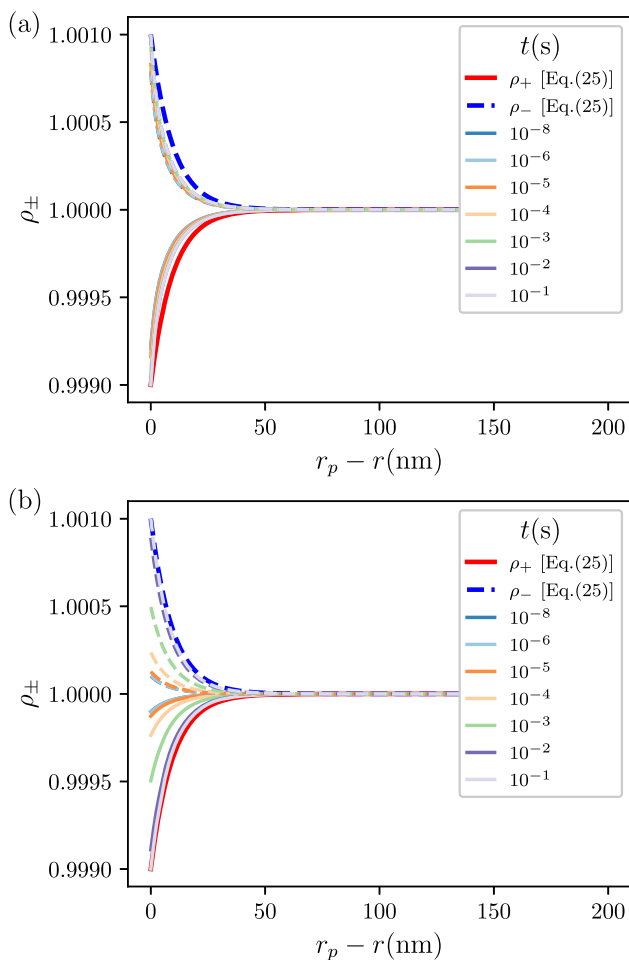


FIG. 10. Evolution of normalized cation (solid lines) and anion (dashed lines) densities along the r axis at the orifice for different reservoir sizes of (a) $r_r = 10 \mu\text{m}$ and (b) $r_r = 200 \text{ nm}$ under applied potentials Φ for an electrolyte concentration of $c_b = 10^{-3} \text{ M}$. The other parameters are set to $\ell_p = 10 \mu\text{m}$, $r_p = 200 \text{ nm}$, $\ell_r = 10 \mu\text{m}$, $\Phi = 10^{-3}$, and $a = 0.1625 \text{ nm}$.

the smallest Dukhin number $\eta = 0.52$, which explains the decent agreement between the analytical and numerical results observed in Fig. 9(a) for that Φ value. Conversely, $\Phi = 4$ yields $\eta = 1.43$, and $O(\eta^2)$ terms are thus no-longer small compared to the other terms in Eq. (23), which are $O(\eta)$ and $O(1)$. This explains the discrepancies in Fig. 9(a) between Eq. (23) and the numerical solutions at $\Phi = 4$. As $\eta \propto c_b^{-1/2}$, one would expect the agreement between Eq. (23) and the numerical solutions to improve with increasing c_b , which we, indeed, observe below (cf. Fig. 11).

For the narrow reservoir ($R/R_b = 2$), the agreement in Fig. 9(b) between the numerics and Eq. (23) is much worse than in Fig. 9(a). This was already anticipated in Ref. 32. The model therein did not explicitly treat the reservoir but instead postulated the ionic number density at the pore mouth ($z = 0$) to instantaneously adapt to the equilibrium Gouy–Chapman solution,

$$\rho_{\pm}(x) = \left(\frac{1 + \tanh(\Phi/2) \exp(-x/\lambda)}{1 - \tanh(\Phi/2) \exp(-x/\lambda)} \right)^{\mp 2}, \quad (25)$$

with x being the distance from the electrode surface. Reference 32 suggested that this postulate would work better for a larger R/R_b —which we, indeed, observe now in Fig. 9—as this implies that the reservoir is essentially in quasi-equilibrium while the pore charges. To explicitly check the validity of the postulate in Ref. 32, in Fig. 10, we compare Eq. (25) for $x = r_p - r$ to MPNP density profiles at the orifice ($z = 0$) for the case of (a) a wide and (b) a narrow reservoir. We see that $\rho_{\pm}(r_p - r, z = 0, t)$, indeed, approach their steady-state profiles much faster for the wide than for the narrow reservoir. For the wide reservoir, the density profiles at the orifice are almost equilibrated at $t = 10^{-8} \text{ s}$, while the rest of the pore relaxes five orders of magnitude slower with $\tau_1 = 2.89 \times 10^{-3} \text{ s}$. From the point of view of the rest of the pore, the orifice thus relaxes instantaneously. Finally, we note that the late-time ion densities are closer to the Gouy–Chapman prediction for the narrow than for the wide reservoir. While postulating instantaneously-relaxed ion densities at the orifice may thus be justified when $R \gg R_b$, these densities may deviate slightly from those deeper in the pore.

In Fig. 11, we again consider various potentials, now for three different c_b . As anticipated, Eq. (23) describes the numerical

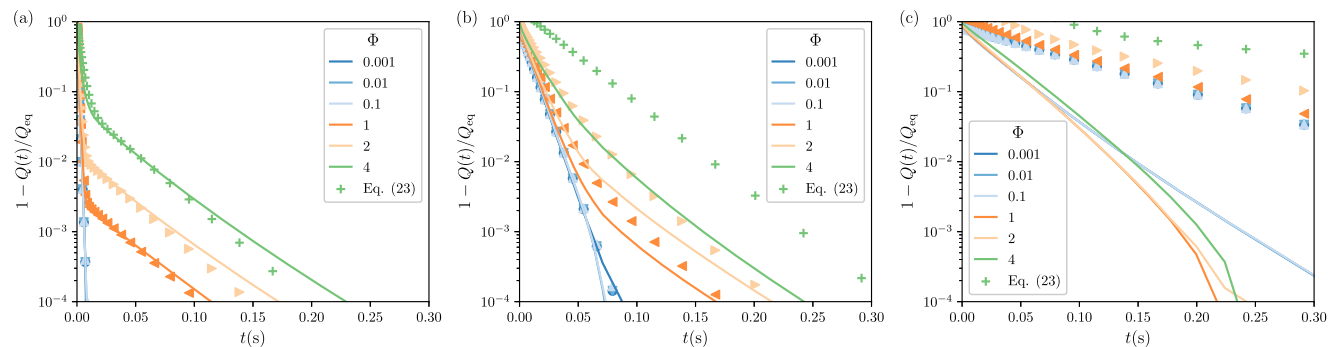


FIG. 11. Surface charge relaxation at different values of applied potentials Φ at electrolyte concentrations of (a) 10^{-2} M , (b) 10^{-4} M , and (c) 10^{-6} M . The other parameters are set to $\ell_p = 10 \mu\text{m}$, $\ell_r = 10 \mu\text{m}$, $r_p = 200 \text{ nm}$, and $a = 0.1625 \text{ nm}$.

solutions better at higher c_b . For $c_b = 10^{-2}$ M, we see in Fig. 11(a) that the pore relaxes biexponentially with two vastly different timescales. Here, Eq. (23) describes the numerical solutions even at $\Phi = 4$, for which, now, $\eta = 0.45$ is, indeed, still smallish. For $c_b = 10^{-4}$ M, we see in Fig. 11(b) that the pore still relaxes biexponentially, but that two timescales differ less than for $c_b = 10^{-6}$ M [Fig. 11(c)]. We understand this with Eq. (23), wherein τ_I decreases with c_b , while τ_{II} does not depend on it. For $c_b = 10^{-6}$ M, we see that analytical and numerical predictions for $1 - Q(t)/Q_{eq}$ do not agree at all.

VI. CONCLUSIONS

Numerically solving the modified Poisson–Nernst–Planck (MPNP) equations, we have studied the charging dynamics of two cylindrical electrolyte-filled pores on either side of a cylindrical electrolyte reservoir, subject to a sudden potential difference. The pores charge exponentially with different timescales, whose dependence on the various system parameters we scrutinized.

For small applied potentials, we found quantitative agreement between our numerical solutions of the MPNP equations and the analytical result by Janssen²⁴ for the bulk-resistance dependence of the TL timescale, both for overlapping and nonoverlapping EDLs. We showed that, contrary to conventional wisdom,^{27,34} the potential in the reservoir is not linear when the reservoir is wider than the pore: it decays much faster into the reservoir. We also discussed the influence of the reservoir resistance on the early-time charging behavior of our system: for $R/R_b \gg 1$, we recovered the known $Q \propto \sqrt{t}$ charging of Ref. 28; for $R/R_b \sim 1$, we found a new linear scaling behavior $Q \propto t$. In several ways, our work, thus, highlights the importance of the electrolyte reservoir on the pore's charging dynamics, which was ignored in many prior studies. Furthermore, we compared Posey and Morozumi's TL equation solution to our MPNP data and found that their solution generally works well at late times and in the interior of the pore; differences between the MPNP data and the TL model were visible at early times and especially near the pore's orifice. Future TL models should, thus, pay close attention to the boundary and initial conditions used.

For moderately strong applied potentials, we compared our numerical solutions to a recent theoretical prediction of Aslyamov and Janssen.³² We found good agreement between these methods for small Dukhin numbers η , but only if the pore resistance R was vastly greater than the reservoir resistance R_b . Discrepancies between these methods for $R \sim R_b$ were traced to the postulate in Ref. 32 that the density profiles at the pore's orifice relax instantaneously, which we showed to be reasonable only for $R \gg R_b$. Future work could, thus, try to generalize the findings of Ref. 32 for cases where $R \sim R_b$. We hope that the insights from our numerical study motivate further work, not only on improved theoretical models but also on new experiments that probe porous electrode charging at the single-pore level.

SUPPLEMENTARY MATERIAL

See the [supplementary material](#) for the effects of the pore cap, pore size parameters, and ionic diameter on the pore charging process.

ACKNOWLEDGMENTS

This work was sponsored by the National Natural Science Foundation of China (Grant No. 22078088) and the Shanghai Rising-Star Program (Grant No. 21QA1401900). This work was also part of the D-ITP consortium, a program of the Netherlands Organization for Scientific Research (NWO) that is funded by the Dutch Ministry of Education, Culture and Science (OCW). J.Y. acknowledges the Chinese Scholarship Council for a visiting fellowship. C.L. and R.v.R. acknowledge the EU-FET project NANOPHLOW (Grant No. REP-766972-1) and helpful discussion with Professor Honglai Liu and Willem Boon. The authors thank Timur Aslyamov for his useful comments on the manuscript.

AUTHOR DECLARATIONS

Conflict of Interest

The authors have no conflicts to disclose.

Author Contributions

J.Y. and M.J. contributed equally to this work.

DATA AVAILABILITY

The data that support the findings of this study are available from the corresponding author upon reasonable request.

REFERENCES

- 1 P. Takhistov, *Biosens. Bioelectron.* **19**, 1445 (2004).
- 2 A. C. Forse, C. Merlet, J. M. Griffin, and C. P. Grey, *J. Am. Chem. Soc.* **138**, 5731 (2016).
- 3 C. Zhan, C. Lian, Y. Zhang, M. W. Thompson, Y. Xie, J. Wu, P. R. C. Kent, P. T. Cummings, D.-e. Jiang, and D. J. Wesolowski, *Adv. Sci.* **4**, 1700059 (2017).
- 4 H. Shao, Y.-C. Wu, Z. Lin, P.-L. Taberna, and P. Simon, *Chem. Soc. Rev.* **49**, 3005 (2020).
- 5 D. Brogioli, *Phys. Rev. Lett.* **103**, 058501 (2009).
- 6 S. K. Patel, C. L. Ritt, A. Deshmukh, Z. Wang, M. Qin, R. Epsztein, and M. Elimelech, *Energy Environ. Sci.* **13**, 1694 (2020).
- 7 C. Lian, M. Janssen, H. Liu, and R. van Rooij, *Phys. Rev. Lett.* **124**, 076001 (2020).
- 8 D. Qu and H. Shi, *J. Power Sources* **74**, 99 (1998).
- 9 M. Eikerling, A. A. Kornyshev, and E. Lust, *J. Electrochem. Soc.* **152**, E24 (2005).
- 10 A. Lasia, *Electrochemical Impedance Spectroscopy and its Applications* (Springer, 2014).
- 11 X. Wang, A. Y. Mehandzhyski, B. Arstad, K. L. Van Aken, T. S. Mathis, A. Gallegos, Z. Tian, D. Ren, E. Sheridan, B. A. Grimes *et al.*, *J. Am. Chem. Soc.* **139**, 18681 (2017).
- 12 A. C. Forse, J. M. Griffin, C. Merlet, J. Carretero-Gonzalez, A.-R.O. Raji, N. M. Trease, and C. P. Grey, *Nat. Energy* **2**, 16216 (2017).
- 13 R. Tivony, S. Safran, P. Pincus, G. Silbert, and J. Klein, *Nat. Commun.* **9**, 4203 (2018).
- 14 S. Kondrat, P. Wu, R. Qiao, and A. A. Kornyshev, *Nat. Mater.* **13**, 387 (2014).
- 15 Y. He, R. Qiao, J. Vatamanu, O. Borodin, D. Bedrov, J. Huang, and B. G. Sumpter, *J. Phys. Chem. Lett.* **7**, 36 (2016).
- 16 K. Breitsprecher, M. Abele, S. Kondrat, and C. Holm, *J. Chem. Phys.* **147**, 104708 (2017).
- 17 K. Breitsprecher, C. Holm, and S. Kondrat, *ACS Nano* **12**, 9733 (2018).
- 18 T. Mo, S. Bi, Y. Zhang, V. Presser, X. Wang, Y. Gogotsi, and G. Feng, *ACS Nano* **14**, 2395 (2020).

- ¹⁹S. Bi, H. Banda, M. Chen, L. Niu, M. Chen, T. Wu, J. Wang, R. Wang, J. Feng, T. Chen *et al.*, *Nat. Mater.* **19**, 552 (2020).
- ²⁰C. Péan, C. Merlet, B. Rotenberg, P. A. Madden, P.-L. Taberna, B. Daffos, M. Salanne, and P. Simon, *ACS Nano* **8**, 1576 (2014).
- ²¹V. S. Daniel-Bekkh, *Zh. Fiz. Khim. SSR* **22**, 697 (1948).
- ²²O. S. Ksenzhek and V. V. Stender, *Dokl. Akad. Nauk SSSR* **106**, 487 (1956).
- ²³R. de Levie, *Electrochim. Acta* **8**, 751 (1963).
- ²⁴M. Janssen, *Phys. Rev. Lett.* **126**, 136002 (2021).
- ²⁵F. A. Posey and T. Morozumi, *J. Electrochem. Soc.* **113**, 176 (1966).
- ²⁶A. Gupta, P. J. Zuk, and H. A. Stone, *Phys. Rev. Lett.* **125**, 076001 (2020).
- ²⁷F. Henrique, P. J. Zuk, and A. Gupta, *Soft Matter* **18**, 198 (2021).
- ²⁸H. Sakaguchi and R. Baba, *Phys. Rev. E* **76**, 011501 (2007).
- ²⁹J. Lim, J. D. Whitcomb, J. G. Boyd, and J. Varghese, *Comput. Mech.* **43**, 461 (2009).
- ³⁰M. Mirzadeh and F. Gibou, *J. Comput. Phys.* **274**, 633 (2014).
- ³¹M. Mirzadeh, F. Gibou, and T. M. Squires, *Phys. Rev. Lett.* **113**, 097701 (2014).
- ³²T. Aslyamov and M. Janssen, *Electrochimica Acta* **167**, 140555 (2022).
- ³³D. B. Robinson, C.-A. M. Wu, and B. W. Jacobs, *J. Electrochem. Soc.* **157**, A912 (2010).
- ³⁴P. M. Biesheuvel and M. Z. Bazant, *Phys. Rev. E* **81**, 031502 (2010).
- ³⁵S. M. Rezaei Niya and J. Andrews, *Electrochim. Acta* **402**, 139534 (2022).
- ³⁶M. S. Kilic, M. Z. Bazant, and A. Ajdari, *Phys. Rev. E* **75**, 021503 (2007).
- ³⁷T. Aslyamov, K. Sinkov, and I. Akhatov, *Nanomaterials* **12**, 587 (2022).
- ³⁸M. Z. Bazant, K. Thornton, and A. Ajdari, *Phys. Rev. E* **70**, 021506 (2004).
- ³⁹M. Janssen and M. Bier, *Phys. Rev. E* **97**, 052616 (2018).
- ⁴⁰I. Palaia, “Charged systems in, out of, and driven to equilibrium: From nanocapacitors to cement,” Ph.D. thesis, Université Paris Saclay (COMUE), 2019.
- ⁴¹A. J. Asta, I. Palaia, E. Trizac, M. Levesque, and B. Rotenberg, *J. Chem. Phys.* **151**, 114104 (2019).
- ⁴²M. Janssen, E. Griffioen, P. M. Biesheuvel, R. van Roij, and B. Ern e, *Phys. Rev. Lett.* **119**, 166002 (2017).
- ⁴³M. S. Kilic, M. Z. Bazant, and A. Ajdari, *Phys. Rev. E* **75**, 021502 (2007).